

Disorders of the Nervous System

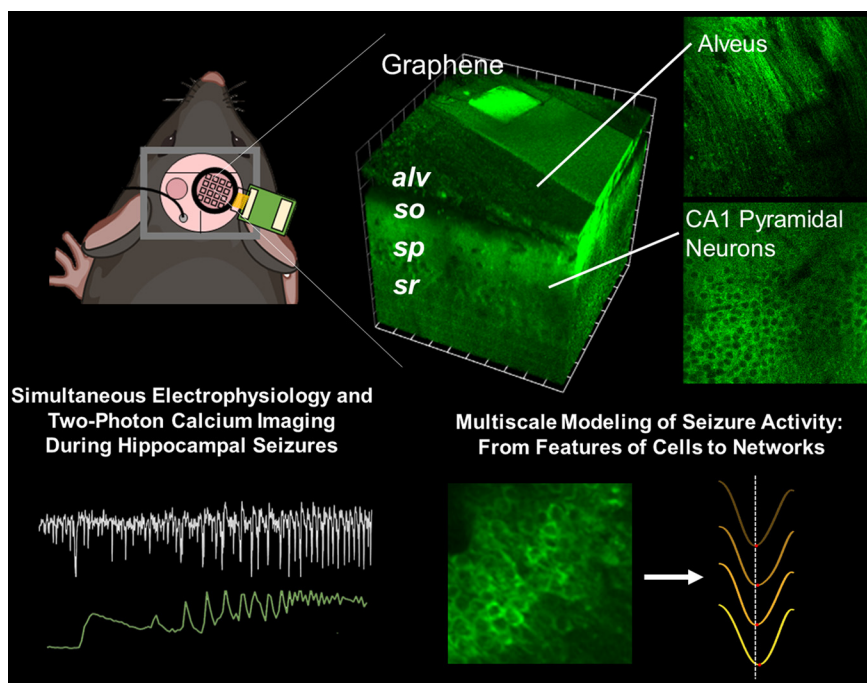
Multimodal, Multiscale Insights into Hippocampal Seizures Enabled by Transparent, Graphene-Based Microelectrode Arrays

Patrick J. Mulcahey,^{1,2}  Yuzhang Chen,^{3,4,5} Nicolette Driscoll,^{2,4,5} Brendan B. Murphy,^{2,4,5} Olivia O. Dickens,⁶ A. T. Charlie Johnson,⁷ Flavia Vitale,^{2,4,5,8,9} and  Hajime Takano^{1,8}

<https://doi.org/10.1523/ENEURO.0386-21.2022>

¹Division of Neurology, Department of Pediatrics, The Children's Hospital of Philadelphia, Philadelphia, PA 19104, ²Department of Bioengineering, University of Pennsylvania, Philadelphia, PA 19104, ³Department of Neuroscience, Perelman School of Medicine, University of Pennsylvania, Philadelphia, PA 19104, ⁴Center for Neuroengineering and Therapeutics, University of Pennsylvania, Philadelphia, PA 19104, ⁵Center for Neurotrauma, Neurodegeneration, and Restoration, Corporal Michael J. Crescenz Veterans Affairs Medical Center, Philadelphia, PA 19104, ⁶Graduate Group in Biochemistry and Molecular Biophysics, University of Pennsylvania, Philadelphia, PA 19104, ⁷Department of Physics and Astronomy, University of Pennsylvania, Philadelphia, PA 19104, ⁸Department of Neurology, Perelman School of Medicine, University of Pennsylvania, Philadelphia, PA 19104, and ⁹Department of Physical Medicine and Rehabilitation, University of Pennsylvania, Philadelphia, PA 19104

Visual Abstract



Hippocampal seizures are a defining feature of mesial temporal lobe epilepsy (MTLE). Area CA1 of the hippocampus is commonly implicated in the generation of seizures, which may occur because of the activity of endogenous cell populations or of inputs from other regions within the hippocampal formation. Simultaneously observing activity at the cellular and network scales *in vivo* remains challenging. Here, we present a novel technology for simultaneous electrophysiology and multicellular calcium imaging of CA1 pyramidal cells (PCs) in mice enabled by a transparent graphene-based microelectrode array (Gr MEA). We examine PC firing at

Significance Statement

There is a pressing need to develop novel technological strategies to integrate modalities toward greater mechanistic understanding of neuronal activities and brain computer interfacing applications. Our study provides an important advance by introducing a cannula imaging window/transparent electrode assembly to perform simultaneous multimodal measurements within mouse hippocampus. Performing and making sense of simultaneous measurements from the scale of single cells to a network level remains a substantial technical and conceptual challenge. Coupling measurements made by our methodology with an interpretable machine learning algorithm allows us to overcome this problem and posit a role of inhibition during hippocampal seizures.

seizure onset, oscillatory coupling, and the dynamics of the seizure traveling wave as seizures evolve. Finally, we couple features derived from both modalities to predict the speed of the traveling wave using bootstrap aggregated regression trees. Analysis of the most important features in the regression trees suggests a transition among states in the evolution of hippocampal seizures.

Key words: calcium imaging; epilepsy; hippocampus; microelectrode

Introduction

Seizures are the hallmark feature of epilepsy, a neurologic disorder that affects 2.2 million people in the United States alone (England et al., 2012). Temporal lobe epilepsy (TLE) is the most common form of epilepsy, accounting for ~60% of all epilepsy patients. Approximately 80% of TLE patients are diagnosed with mesial TLE (MTLE), an epilepsy subtype that implicates the hippocampus and the surrounding brain regions in the generation of often drug-refractory seizures (Lévesque et al., 2018). Despite the high clinical prevalence of MTLE, the mechanisms of seizure initiation and evolution in the hippocampus remain poorly understood.

Of the subfields of the hippocampus, CA1 has historically been regarded as an important site for seizure initiation and evolution. In the broader context of the hippocampal-entorhinal system, CA1 often succumbs to seizure-promoting

inputs from CA3 and the entorhinal cortex (Dulla et al., 2018). Early work in *in vitro* slice models of seizure-like events implicated the CA3-CA1 axis in the generation of epileptiform activity. In these models, slices are bathed in solutions with an ionic imbalance (low Mg^{2+} , Cl^- , high K^+) or pharmacological convulsants [picrotoxin, 4aminopyridine (4-AP)], resulting in spontaneous discharges that originate in CA3, propagate along the highly recurrent, excitatory Schaffer collaterals, and induce a depolarization associated with a burst of action potentials in the cell populations of CA1 (Dulla et al., 2018). Moreover, voltage sensitive dye imaging studies in rodent epileptic hippocampal slices demonstrated a substantial upregulation of the excitatory input of the temporoammonic pathway from entorhinal cortex layer III to CA1 (Ang et al., 2006). At the cellular scale in area CA1, there has been a substantial focus on pathologic activity inducing the development of “burster” neuron populations in epilepsy (Jensen and Yaari, 1997; Chen et al., 2011; Takano et al., 2012). In epileptic CA1, a fraction of the pyramidal cell (PC) population converts from regular firing modes (the predominant spiking mode in normal conditions) to a bursting mode. In the bursting mode, cells may fire action potentials spontaneously or in dense clusters in response to threshold stimulation. Importantly, bursting PC neurons can initiate network bursts in CA1 and are thought to play a significant role in the initiation of epileptiform events.

These insights, predominately derived from *in vitro* studies of the hippocampus, emphasize the multiscale nature of epileptic activity in CA1. Seizures may either be driven both by the endogenous populations of excitable cells in CA1 or by network level interactions with the structures that innervate it. Relating these scales of activity *in vivo* in the hippocampus remains both a significant technical and conceptual challenge. Electrophysiology is the gold standard technique for recording seizures, but electroencephalography (EEG) lacks the fine spatial resolution required to resolve the activity of CA1 microcircuits (Farrell et al., 2019). Single or multishank high-density laminar probes can resolve the activity of microcircuits

Received September 21, 2021; accepted April 15, 2022; First published April 25, 2022.

The authors declare no competing financial interests.

Author contributions: P.J.M., F.V., and H.T. designed research; P.J.M., Y.C., N.D., B.B.M., O.O.D., and H.T. performed research; A.T.C.J. contributed unpublished reagents/analytic tools; P.J.M. analyzed data; P.J.M. and H.T. wrote the paper.

This work was also supported by the National Institutes of Health Grant R21-NS106434 (to H.T. and F.V.), the Citizens United for Research in Epilepsy Taking Flight Award (F.V.), and the National Science Foundation Grant MRSEC DMR-1720530 (to A.T.C.J.). This work was supported by the National Science Foundation Graduate Research Fellowship Program Grant DGE-1845298; to P.J.M., N.D., B.B.M.) and was carried out in part at the Singh Center for Nanotechnology, which is supported by the National Science Foundation's National Nanotechnology Coordinated Infrastructure Program Grant NNCI-1542153.

Acknowledgements: We thank Douglas A. Coulter, Christopher D. Adam, and Srdjan M. Joksimovic for their feedback on this work.

Correspondence should be addressed to Hajime Takano at takanoh@chop.edu.

<https://doi.org/10.1523/ENEURO.0386-21.2022>

Copyright © 2022 Mulcahey et al.

This is an open-access article distributed under the terms of the Creative Commons Attribution 4.0 International license, which permits unrestricted use, distribution and reproduction in any medium provided that the original work is properly attributed.

but cannot resolve the behavior of individual cells during seizure, as local hypersynchrony and changes in action potential waveform shape following seizure recruitment render spike sorting intractable (Merricks et al., 2015). Cellular imaging techniques, such as two-photon multicellular calcium imaging, can resolve the behavior of genetically defined neural populations with single cell resolution, although they sacrifice the temporal resolution of electrophysiology (Yaksi and Friedrich, 2006; Takano and Coulter, 2012). Single-scale observations of the hippocampus during seizure inherently limit our conceptual understanding of how these scales interact. For example, in cortical epilepsy, multiscale, nonlinear models of seizure activity were developed only after simultaneous macroscale electrocorticography and Utah microarray recordings were introduced clinically (Eissa et al., 2017; Schevon et al., 2019). To overcome the technical limitations of single-modality measurements, transparent microelectrode arrays (MEAs) have emerged in recent years as a family of novel neurotechnologies that enable simultaneous electrophysiology and calcium imaging (Kuzum et al., 2014; Park et al., 2014; Driscoll et al., 2021; Liu et al., 2021). Previously, low-magnification calcium imaging combined with a transparent MEA recordings in 4-aminopyridine-induced cortical seizures revealed the evolution of hidden modes throughout seizure recruitment, evolution, and termination (Driscoll et al., 2021). In particular, this study emphasized the unique contribution of widefield calcium imaging, whose slow propagation and evolution resembled the spread of a core seizure-recruited territory, or “ictal core,” to electrophysiological recording of seizures.

To address these challenges, we propose a novel methodology for simultaneous electrophysiological recording and two-photon multicellular calcium imaging of CA1 PCs during acutely-induced seizures *in vivo*. Our strategy is enabled by fabricating an implantable imaging window integrated with an optically transparent MEA based on graphene. This methodology allows us to image the activity of hundreds of neurons within a $300 \times 300 \mu\text{m}^2$ area while recording electrical signals from an area covering $1.55 \times 1.55 \text{ mm}^2$. Bridging modalities and scales, we examine the recruitment of PCs at seizure onset, the oscillatory organization of neural ensembles during the established seizure, and the spatio-temporal characteristics of the low-frequency seizure traveling wave throughout seizure evolution. Finally, we combine features derived from multicellular calcium imaging and single site electrophysiology to predict the speed of the seizure traveling wave using bootstrap aggregated regression trees. By examining the time evolution of the most important features in the regression trees, we note substantial changes in feature values coincident with changes in the speed of the traveling wave, suggesting a dynamic transition through states as seizures evolve and terminate in CA1.

Materials and Methods

All animal use was performed in accordance and with the approval of the Children’s Hospital of Philadelphia’s Institutional Animal Care and Use Committee. A total of

11 mice of either sex were used in this study. Four mice expressing genetically encoded calcium indicators were implanted with transparent MEAs, resulting in three high-quality multimodal datasets and one calcium imaging-only dataset. Seven wild-type mice were implanted with 32-channel multishank probes, resulting in seven high-quality electrophysiology-only datasets.

Multimodal recordings with graphene-based MEAs (Gr MEAs)

Transparent, flexible MEAs based on graphene were fabricated as described previously (Driscoll et al., 2021). The impedance of the graphene channels was $1.95 \pm 0.33 \text{ M}\Omega$ (mean \pm SD). First, a 3-mm cover glass imaging window (Warner CS-3R-0) was affixed to a custom-made, hat-shaped steel cannula with an outer diameter of 3 mm (University of Pennsylvania, Vision Research Center Machine Shop) using Norland Optical Adhesive NOA 60 (Edmund Optics). Then, graphene devices were secured to the cover glass surface using the same adhesive. Eight- to 12-week-old mice expressing genetically encoded calcium indicators ($n = 4$, C57BL6-Thy1-GCaMP6s and C57BL6-Thy1-jRGECO1a, The Jackson Laboratory) were anesthetized with isoflurane anesthesia (1–2%) in oxygen. A stainless-steel screw attached to silver wire was implanted bilaterally in the skull above the right cerebellum, and a metal headplate (Narishige USA) was fixed to the skull with dental acrylic (Lang Dental). In the left hemisphere, a 2.0-mm diameter craniotomy was drilled, and the dura was removed (anteroposterior: $\sim -1.0 \text{ mm}$, mediolateral: $\sim -2.0 \text{ mm}$). In the right hemisphere, a 3.0-mm diameter craniotomy was drilled, and the dura was removed (anteroposterior: $\sim -2.0 \text{ mm}$, mediolateral: $\sim 2.0 \text{ mm}$). The cortex was gently aspirated with constant application of artificial CSF (ACSF; in mM, 125 NaCl, 2.5 KCl, and 1.25 NaH_2PO_4) to reveal the fibers of the alveus.

Following completion of the surgery, the anesthetic was switched to ketamine/xylazine (100/10 mg/kg), and the headplate was attached to a small imaging platform (Narishige USA). This platform was mounted on a fixed stage, and imaged with a two-photon microscope (Thorlabs Bergamo Scope). For imaging, the field was centered over a graphene electrode pad using a $16\times$ objective (Nikon, 0.8 N.A., 3 mm WD). The objective was then lowered until CA1 pyramidal neurons could readily be visualized in the field. GCaMP6s was excited at 920 nm and jRGECO1a was excited at 1040 nm with a femtosecond-pulsed two photon laser (Mai Tai DeepSee, Spectra-Physics). Images were captured in a single plane at a constant acquisition rate between 5 and 10 Hz. To block ambient light, all imaging sessions were performed with the microscope enclosed in a dark chamber. The imaging data were captured in binary format and converted to TIF format on a PC, and timing of electrophysiological recording and imaging was synched by a TTL signal. The MEA was connected to a custom connector that interfaced with the Smartbox V2 (Neuronexus). For recording, the graphene electrode array, a custom connector, and the headstage (SmartLink16, NeuroNexus)

were attached to a stainless-steel bar/micromanipulator ensemble. Electrophysiological data were sampled at 20 kHz via the headstage and the controller (SmartBox, NeuroNexus), and the data were saved to a PC in an Intan file format. A 5-min epoch of baseline activity was recorded and imaged before seizure induction. Seizures were induced pharmacologically by manually applying 20 μ l of 4°C 15 mM 4-AP in ACSF to the cortical surface exposed by the left portal craniotomy. Hippocampal activity was recorded continuously for 2–3 h after application of 4-AP. At the end of experiments, image stacks of the area underneath the graphene device/imaging window were captured *in vivo* in the two-photon microscope.

Multishank probe recordings

Eight- to 12-week-old C57BL/6 mice ($n=7$, The Jackson Laboratory) were anesthetized with isoflurane anesthesia (1–2%) in oxygen. Two stainless steel screws attached to silver wires were implanted bilaterally in the skull above the cerebellum, and a metal headplate (Narishige USA) was fixed to the skull with dental acrylic (Lang Dental). In the left hemisphere, a 2.0-mm diameter craniotomy was drilled, and the dura was removed (anteroposterior: \sim –1.0 mm, mediolateral: \sim –2.0 mm). In the right hemisphere, a rectangular craniotomy was drilled, and the dura was removed (anteroposterior: \sim –2.0 mm, mediolateral: \sim 2.0 mm). The anesthetic was then switched to ketamine/xylazine (100/10 mg/kg), and the headplate was attached to a small platform (Narishige USA). A 32-channel multishank probe (Neuronexus A4x8-5 mm-200–400–177–A32) sensitized with 25 mg/ml 1,1'-dioctadecyl 3,3,3',3' (Dil; Thermo Scientific) in ethanol was targeted to the right dorsal hippocampus (anteroposterior: \sim –2.0 mm, mediolateral: \sim 0.7 mm, dorsoventral: \sim –2.0 mm). Contacts for the ground and reference were made contralateral and ipsilateral to the recording site, respectively. Recordings were sampled at 20 kHz via the Neuronexus Acute Smartlink32 Headstage and Smartbox. Following 10 min of baseline recording, 20 μ l of 4°C 15 mM 4-AP in ACSF (in mM, 125 NaCl, 2.5 KCl, and 1.25 NaH₂PO₄) was applied to the exposed cortex contralateral to the recording site, as during recordings made with the Gr MEA. Hippocampal activity was recorded continuously for 2–3 h after application of 4-AP. After completion of the recordings, mice were transcardially perfused with sucrose-rich ACSF (in mM, 75 sucrose, 87 NaCl, 2.5 KCl, 1.25 NaH₂PO₄, 10 glucose, 26 NaHCO₃, 2 CaCl₂·H₂O, and 1 MgSO₄) and decapitated under deep isoflurane anesthesia. Brains were removed and submerged in ice cold sucrose-rich ACSF. Coronal hippocampal slices (400 μ m thick) were cut using a Vibratome VT1200S (Leica). Slices were imaged using an Olympus FV10000 confocal microscope (Olympus Corporation) with a 543-nm excitation wavelength (Melles Griot). Multishank probe locations were then co-registered with the Allen Brain Atlas using a custom-written MATLAB script (R2019b MathWorks).

Analysis of the electrophysiological and imaging data

All data analysis was performed in MATLAB R2019b. Statistical analyses were performed in MATLAB R2019b or

Prism 9 (GraphPad). To facilitate the reproducibility of this work, all custom-written MATLAB code used for analysis is available on GitHub at www.github.com/mulcaheyp. Only data obtained from graphene microelectrodes with 1000-Hz impedance between 900 k Ω and 5 M Ω were considered for analysis. Only data obtained from multishank probe channels localized to CA1 (stratum oriens, stratum pyramidale, stratum radiatum, stratum lacunosum moleculare) were considered for analysis.

Calcium transient onset analyses

All calcium imaging data were registered in Suite2P. Circular regions of interest (ROIs) were manually drawn in FIJI (ImageJ, NIH) around putative CA1 PCs. To minimize the intrusion of the neuropil signal, we performed ROI shrinking by decreasing the ROI by two pixels using a custom Java macro (Wenzel et al., 2017, 2019). Fluorescence traces were extracted from the images, imported into MATLAB, normalized to baseline (preseizure) values and filtered with a second-order Savitzky–Golay filter with a window length of 7. A window of 40–100 frames was segmented off containing the optical onset of the seizure determined by examining population-wide increases in calcium fluorescence. An onset threshold for each cell was set as the mean + 5*SD of the baseline signal of the 25 frames immediately preceding the beginning of the window. The onset time for each cell was extracted as the frame where the fluorescence amplitude first exceeded the threshold. The recruitment duration was calculated as the time difference between the last detected cellular onset and the first detected cellular onset. The SD of the recruitment durations was calculated over all seizures for all four animals. A total of 17 seizures over four animals were used for the recruitment duration analyses.

For the reliability analyses, we restricted our analyses to seizures captured in common imaging planes; 15 seizures over four animals were used for these analyses ($n=3, 4, 2, 6$ seizures in each animal). We examined the reliability of the cellular recruitments between seizures by calculating pairwise Spearman's rank correlation coefficients for the cell rank vectors from pairs of seizures for each animal. We further examined cellular onset reliability by calculating Kendall's coefficient of concordance between rank vectors obtained from all seizures in each of the four animals. To obtain p values for the Kendall's coefficients, we calculated the Kendall's coefficients for 1000 randomly shuffled rank matrices, where the cells in each seizure were randomly assigned ranks between 1 and the maximum rank observed for a given seizure. The p value for the observed Kendall's coefficient was determined by calculating the fraction of randomly-generated Kendall's coefficients that exceeded the observed Kendall's coefficient.

In three seizures, we calculated vectors to represent the direction of the seizure onset in calcium imaging for later comparison with the direction of the electrophysiological seizure traveling wave (see below). We calculated these vectors as a difference between two points in 2D space, $x_2 - x_1$. To determine the position of x_1 , we extracted and averaged the locations of all ROIs that had an onset rank of "1" for a particular seizure. To determine the position of x_2 , we extracted and average the locations of all ROIs

that had the maximum onset rank for a particular seizure. To transform the vector to anatomic space, we reflected it about the x -axis and rotated it 30° toward the y -axis to account for rotation of the experimental animal relative to the camera/optical path. We calculated the direction of the seizure onset vectors by calculating the angle of the vector using the MATLAB command “atan2.” A polar histogram of the seizure onset vector directions was plotted with six bins.

High γ analyses

Electrophysiological data from annotated seizures was imported into MATLAB, down sampled to 2 kHz, and then bandpass filtered in the 4- to 30-Hz (low frequency) and 80- to 150-Hz (high γ) bands using second-order Butterworth filters. The instantaneous phase of the low-frequency signal and the instantaneous amplitude of the high γ signal were calculated using the Hilbert transform. High γ events were detected on individual channels based on a threshold of a mean + 2.5*SD of the high γ amplitude. The phase of the low-frequency component was extracted at each detected high γ amplitude peak. Polar histograms of the low-frequency phase distributions were plotted with 18 bins. We examined whether the phase distributions of the peak high γ amplitudes differed from randomly selected distributions of phases using the Watson–Williams test in the MATLAB Circular Statistics Toolbox (Berens, 2009). In the case that the assumptions of the Watson–Williams test were violated, we used the multisample test for equal median directions.

Multisunit activity (MUA) analyses

Electrophysiological data from annotated seizures was imported into MATLAB and then bandpass filtered in the 4- to 30-Hz (low frequency) and 300- to 3000-Hz (spike) bands using second-order Butterworth filters (Weiss et al., 2013). The instantaneous phase of the low-frequency signal was calculated using the Hilbert transform. MUA was detected by finding negatively-deflecting electrographic events in the spike band that exceeded a threshold, t , of:

$$t = -4 * \text{median} \left(\left| \frac{x(t)}{0.6745} \right| \right), \quad (1)$$

with $x(t)$ as the signal of the spike band (Quiroga et al., 2004). The phase of the low-frequency component was extracted at each detected multisunit event. Polar histograms of the low-frequency phase distributions were plotted with 18 bins. We examined whether the phase distributions of the detected MUA differed from randomly selected distributions of phases using the Watson–Williams test (Berens, 2009). In the case that the assumptions of the Watson–Williams test were violated, we used the multisample test for equal median directions.

Traveling wave analyses

To examine the dynamics of the traveling wave, we adapted an analysis first developed to examine traveling waves in seizures across Utah arrays (Liou et al., 2017). In this analysis, we detected the times of individual seizure

discharges recorded on the Gr MEAs by detecting peaks in the low-frequency (4–30 Hz) signal that exceeded a threshold of 2 SDs above the mean of the absolute value of the low-frequency signal on individual channels. Peaks detected across channels were considered to be part of the same ictal discharge if they occurred within 150 ms of each other, and only peaks that were detected on at least >60% functional channels were considered for analysis. The peak timing was then associated with the location of the microelectrode on the Gr MEA. Each seizure discharge thus was represented by a set of points (x , y , t) with x and y as the locations of the channels on the array and t as the time of peak amplitude of the low-frequency signal. We then fit a plane for each seizure discharge using these sets of points. We used this fit to calculate the gradient of the plane. We then represented the direction of the wave as the angle of the gradient vector calculated by the inverse tangent, and we calculated the speed of the wave as the inverse norm of the vector. We tested the nonuniformity of the distributions of seizure discharge directions using the Omnibus test (Berens, 2009), and we compared the distributions of seizure discharge directions between animals using the Kolmogorov–Smirnov test (Prism 9). To compare the speeds of the vectors at the beginning and end of the seizure, we extracted the speeds of the vectors in the first 25% of the seizure duration and the vectors in the last 25% of the seizure duration. Twelve seizures were subject to the comparisons of traveling wave speeds in the first 25% of the seizure duration and the last 25% of the seizure duration, for a total of twelve individual comparisons. The number of discharges considered in each test were (no. of discharges in first 25% of duration/no. of discharges in last 25% of duration) 121/121, 101/81, 111/117, 33/34, 129/130, 168/169, 205/206, 46/55, 80/88, 83/90, 109/113, and 125/127.

Training bootstrap aggregated regression trees for traveling wave speed prediction

Feature extraction

For this portion of the study, we restricted our analysis to four seizures from three animals with completely uninterrupted electrophysiology and multicellular calcium imaging data. Many seizures recorded multimodally had brief gaps between imaging time series, as the imaging acquisition was performed by capturing only 3000–6000 frames at a time, whereas electrophysiology was collected continuously at 20 kHz. To avoid the loss of information associated with absent imaging data during transitions between imaging series, only seizures captured entirely within an imaging time series were considered for this analysis. Concatenated multimodal data from these seizures was first imported to MATLAB. This data included (1) calcium fluorescence traces from 10–20 PC *somae* from under the putative site of electrophysiological recording; (2) the electrophysiological recording from the channel above the imaging plane; and (3) the electrophysiological recording from all functional channels in the array. In sliding windows of 4-s duration and 1-s overlap, the following features were calculated from the single channel (above

the imaging plane) electrophysiology data: mean high γ amplitude, SD of the high γ amplitude, fractional 4- to 30-Hz power, fractional 80- to 150-Hz power, and the phase locking value (PLV) between the 4- to 30-Hz and 80- to 150-Hz filtered signals. The mean high γ amplitude and the SD of the high γ amplitude were calculated using the amplitude time series derived from the Hilbert transform of the 80- to 150-Hz bandpass filtered (second-order Butterworth) signal in each bin. The fractional band powers were calculated by dividing the integral of the power spectrum over the 4- to 30-Hz or 80- to 150-Hz range by the integral of the entire power spectrum. Finally, PLV was calculated as:

$$PLV = \left| \frac{1}{N} \sum_{n=1}^N \exp(i(\varphi_{4-30Hz}[n] - \varphi_{a(80-150Hz)}[n])) \right|, \quad (2)$$

where φ_{4-30Hz} is the phase of the 4- to 30-Hz bandpass filtered (second-order Butterworth) signal and $\varphi_{a(80-150Hz)}$ is the phase of the instantaneous amplitude of the 80- to 150-Hz bandpass (second-order Butterworth; Weiss et al., 2013). In sliding windows of 4-s duration and 1-s overlap, the following features were calculated from the multicellular calcium imaging data: mean cellular $\Delta F/F_0$ amplitude, mean cellular $\Delta F/F_0$ line length, the SD of the first derivative of the cellular $\Delta F/F_0$, mean cell pair $\Delta F/F_0$ correlation (Pearson's r), and the SD of the cell pair $\Delta F/F_0$ correlations. $\Delta F/F_0$ line length was calculated for each cell as:

$$LL = \sum \left| \frac{d}{dt} \Delta F/F_0 \right|, \quad (3)$$

with $d/dt \Delta F/F_0$ as the first derivative of the $\Delta F/F_0$ time series (Esteller et al., 2001). In each window, the speed of the traveling wave was set to the median of all traveling wave speed observations in the bin. Bins without traveling wave observations were not considered during model training.

Model training and testing

We used features and speeds from three seizures from three different animals as the dataset for model training. We trained 1000 ensembles of 100 bootstrap aggregated regression trees with surrogate decision splits using the curvature test to select the best split predictor. Before model training, we ensured that the training set was equally enriched for features and speeds from all three seizures used in training by randomly selecting bins from the two longest seizures such that the training set consisted of $3 \times k$ observations, with k observations from each seizure. Models were trained with 5-fold cross validation, and the model that best generalized to a withheld fraction of the training set was stored. The importance of each feature was calculated using the "OOBPermutedPredictorDeltaError" property of the bagged regression tree models in MATLAB. For each variable, the feature importance represents the increase in prediction error if the values of that variable were permuted across the out-of-bag observations. This measure is computed for every tree in

the ensemble, averaged over the ensemble, and divided by the SD over the entire ensemble. The performance of the 1000 ensembles was assessed by calculating the Pearson's correlation coefficient between the experimentally observed speeds from the seizures used in the training set and the predicted speeds from the seizures used in the training set. To examine model generalization, we predicted the traveling wave speed in a fourth, withheld seizure. The generalizability of the 1000 ensembles was assessed by calculating the Pearson's correlation coefficient between the experimentally observed speeds from the withheld seizure and the predicted speeds from the withheld seizure. The top 100 (10%) performing models were considered the "best generalizing models." We examined the feature importance, determined as above, in these best generalizing models. For the remaining analyses, we considered the top three most important features in the ensembles of regression trees. The same procedures were performed for 1000 bagged regression trees trained on features derived from only calcium imaging or electrophysiology to compare the performance between single and multimodal models.

Most important feature evolution throughout seizure

We then compared the three most important features values between the first 25% versus last 25% of the seizure duration in all seizures used to construct the models. To compare across records, we rescaled the individual features from separate seizures to a range of 0–1, where the minimum feature value was rescaled to 0 and the maximum feature value was rescaled to 1. We then extracted the rescaled feature values from the first 25% of the sliding windows and the last 25% of sliding windows in each seizure and pooled the distributions. We compared the rescaled features from the first 25% of the seizure duration to the last 25% of the seizure duration using Mann–Whitney U tests in Prism 9.

Results

Multimodal recordings of pharmacologically induced seizures in CA1

Understanding seizure activity in the hippocampus *in vivo* has been hampered by limitations to simultaneously leveraging the high temporal fidelity of electrophysiological recording and the high spatial specificity of single-cell neuronal imaging. We designed an experiment to acutely induce seizures and to simultaneously record broadband hippocampal electrophysiology and image individual CA1 PCs *in vivo* in mice expressing a fluorescent calcium indicator (Fig. 1A). We developed a novel implant strategy based on a transparent 16-channel Gr MEA affixed to an imaging window and 3-mm cannula (Fig. 1B). The MEA consisted of a 4×4 grid of $50 \times 50 \mu\text{m}$ square Gr contacts with 500- μm pitch. This assembly was implanted above the alveus over the right dorsal hippocampus of a mouse expressing a genetically encoded fluorescent calcium indicator mainly in PC populations (Fig. 1C). Two-photon microscopy through the transparent Gr MEA allowed us to resolve the laminar structure of dorsal CA1 (Fig. 1D)

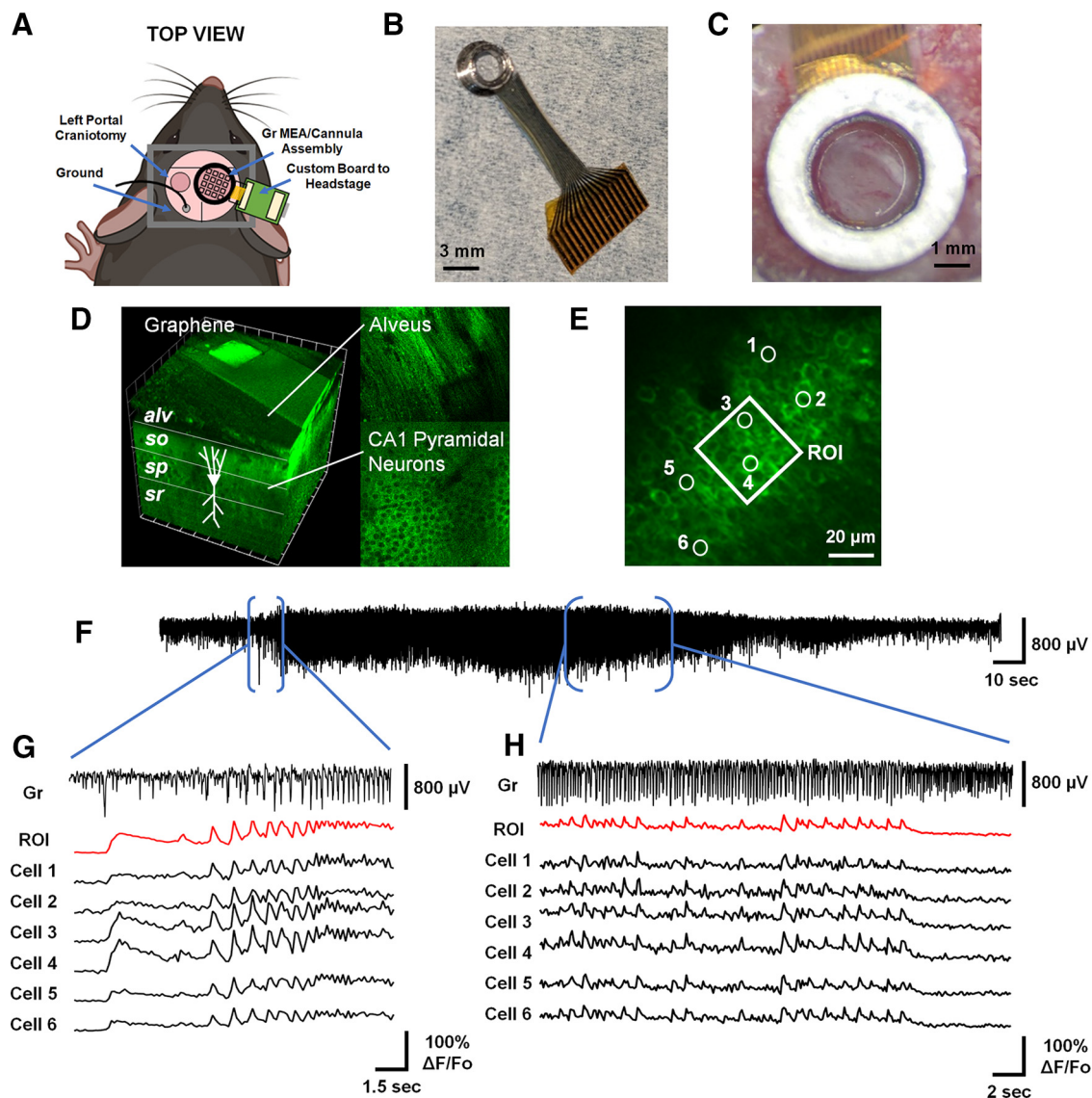


Figure 1. Transparent Gr MEAs enable multimodal recordings of CA1 during acute seizures. **A**, Overview of the experimental preparation for observing hippocampal seizures. A ground screw is implanted in the left cerebellum, and a bar for head fixation is glued to the skull. A left portal craniotomy is drilled for application of 4-AP to induce seizures. A right craniotomy is drilled and the cortex over the alveus is aspirated to enable implantation of the Gr MEA. Adapted from “Mouse (dorsal)” by BioRender.com. **B**, The novel implant strategy consisted of a transparent Gr MEA affixed to an imaging window and 3-mm cannula. **C**, The Gr MEA/imaging window/cannula assembly is implanted over the right alveus fibers. **D**, This configuration permits two-photon multicellular calcium imaging through the alveus (alv) to the layers of dorsal CA1, including stratum oriens (so), stratum pyramidale (sp), and stratum radiatum (sr) in animals expressing a fluorescent calcium indicator. **E**, In the sp, two-photon multicellular calcium imaging can resolve individual CA1 PCs. In this schematic, the square ROI corresponds to the approximate area covered by a single $50 \times 50 \mu\text{m}$ Gr microelectrode, and the numbered circles correspond to individual CA1 PCs. **F**, Following application of 4-AP to the left cortex, seizures later emerge in the right hippocampus (Extended Data Figs. 1-1, 1-2). An example seizure event captured from one Gr microelectrode on the array is displayed. **G**, The MEA/imaging window/cannula assembly enables simultaneous electrophysiology (labeled Gr) and two-photon multicellular calcium imaging (labeled ROI, cells 1–6, with conventions from panel **E** at seizure onset. **H**, Similarly, simultaneous electrophysiology and two-photon multicellular calcium imaging resolves activity across modalities as seizures evolve.

and populations of putative CA1 PCs (circular ROIs; Fig. 1E) under the site of recording (square ROI; Fig. 1E).

We induced seizures in anesthetized mice by bath applying 4-AP in ACSF ($20 \mu\text{l}$, 15 mM , 4°C) to the exposed cortical surface contralateral to the site of recording and imaging (Fig. 1A). This approach allowed us to capture an

hours-long evolution of hippocampal activity as the brain transitioned from a period of ketamine/xylazine-induced burst suppression (Extended Data Fig. 1-1A–C) to recurrent seizures. In approximately half of our experiments ($1/3$ Gr MEA implants, $4/7$ multishank probe implants), we observed spikes and extended epileptiform patterns that

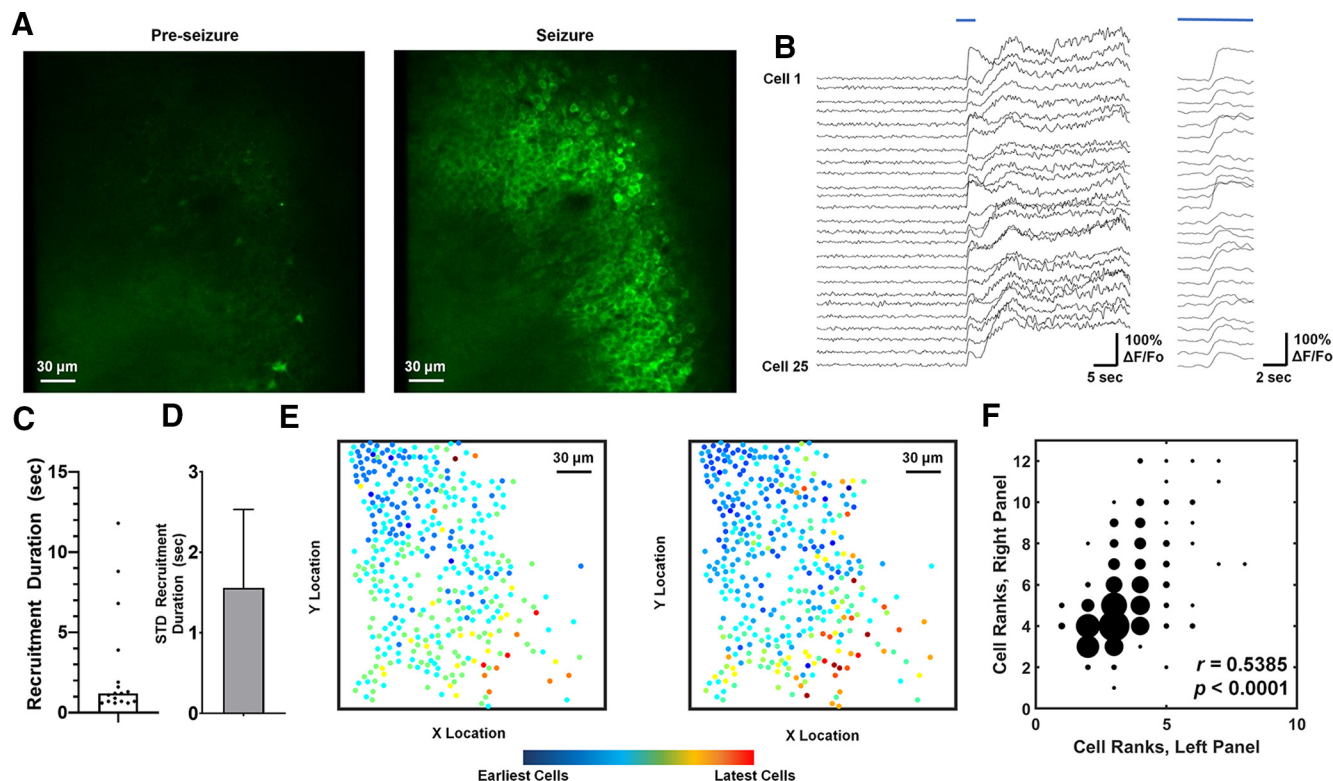


Figure 2. Spatiotemporal characteristics of CA1 PC recruitment to hippocampal seizures. **A**, Two-photon multicellular calcium imaging during seizure is characterized by a population-wide increase in fluorescence relative to pre-seizure baseline. **B**, Representative traces from 25 CA1 PCs at seizure onset (blue line), magnified on the right. **C**, Distribution of recruitment durations ($n = 17$ seizures, 4 animals). **D**, Within-animal recruitment duration variability (shown as the mean STD \pm SEM). The recruitment duration variability does not change with varying threshold (Extended Data Fig. 2-1). **E**, Spatiotemporal maps of cell recruitment in two seizures from the same animal, indicating preserved relative recruitments of PCs. Each dot represents the location of a single cell in the imaging frame. The colorization of the dot indicates the relative time of cell recruitment, with blue dots indicating the earliest-recruited cells and red dots indicating the latest-recruiting cells. **F**, Scatter plot displaying the cell ranks in the seizures displayed in panel **E**. The marker size varies depending on the number of observations at a coordinate, varying from 1 (smallest marker size) to 27 (largest marker size). The Spearman's correlation coefficient for this relationship is 0.5385, with $p < 0.0001$.

emerge before seizures (Extended Data Figs. 1-1D,E, 1-2). All animals exhibited large-amplitude seizures (Fig. 1F; Extended Data Fig. 1-1F), with the first seizure appearing in the right hippocampus at 1.71 ± 0.49 h (mean \pm SD) after application of 4-AP. We restricted our analyses to this activity in this work. Our Gr MEA implant enabled us to concurrently resolve electrophysiological and single cellular calcium fluorescence activity at seizure onset (Fig. 1G) and throughout seizure evolution (Fig. 1H).

Dynamics of PC recruitment to recurrent seizures

Relative to baseline, pre-seizure conditions, seizures were marked by a population-wide increase in calcium fluorescence signal in the field of view (Fig. 2A). Extraction of baseline-normalized calcium fluorescence time series from circular ROIs over putative PC cell bodies allowed us to resolve recruitment of individual PCs to seizure activity (Fig. 2B).

Previous multicellular calcium imaging studies in hippocampus *in vitro* and cortex *in vivo* investigated the time-scale and reproducibility of cellular recruitment patterns during epileptic activity (Takano et al., 2012; Wenzel et al.,

2017). Accordingly, we quantified the absolute recruitment duration and cell recruitment rank reproducibility of optically recorded seizures. We found that the median recruitment duration, defined as the time difference between the first and last detected cellular recruitment time, was 1.2 s (17 seizures captured optically, four animals), with a range of 0.6 s to 11.8 s (Fig. 2C). We quantified the within-animal variability in recruitment duration by calculating the SD (STD) of recruitment durations within individual animals. We found that the mean STD of recruitment duration was 1.56 s, with a range of 0–4.29 s (Fig. 2D). Importantly, the mean STD of recruitment duration was invariant over a range of thresholds for calcium transient onset (Extended Data Fig. 2-1). We used two measures to examine the reproducibility of PC recruitment to recurrent seizures. The outcome measures were (1) the Spearman's rank coefficient (r) between pairs of seizures within an animal and (2) Kendall's coefficient of concordance (W) among seizures within an animal. Both measures are indicators of ranking order consistency in which values of 0 indicate completely inconsistent recruitment ranks and values of 1 indicate totally consistent recruitment ranks between/among seizures. Of all seizure pairs, 92% of pairs

had positive correlations between cell recruitment ranks (23/25 pairs had Spearman's $r > 0$ with $p < 0.05$; see Materials and Methods). The Spearman r between cell recruitment ranks in significantly correlated seizure pairs was 0.489. To visualize an example of the reproducibility of PC recruitment, we display a map of the spatial pattern of relative cell recruitment in two seizures from the same animal in Figure 2E. To provide a visualization of the Spearman's r calculation, we display a scatter plot in Figure 2F in which the x - and y -coordinates are the cell ranks between the two seizures displayed in Figure 2E. The Spearman's r value for this seizure pair was 0.5385. The consistent recruitment order was also supported by significant Kendall's W values for each animal (one per animal, all significant to $p < 0.05$, $W_1 = 0.5439$, $W_2 = 0.3978$, $W_3 = 0.5671$, $W_4 = 0.7238$).

Phase-association of high γ and MUA in CA1 during seizure

Beyond seizure onset, a hallmark feature of brain territories recruited to seizure is the presence of high γ and MUA phase-locked to the local field potential (LFP; Schevon et al., 2012; Weiss et al., 2013, 2015). While the saturation and low sampling frequency of the calcium imaging data limited our ability to resolve activity beyond seizure onset, the high temporal resolution of electrophysiology allowed us to examine and analyze fast activity during seizures. When we filtered the data obtained from the Gr MEA in the LFP (4–30 Hz), high γ (80–150 Hz), and spike (300–3000 Hz) bands, we noted the presence of high γ and MUA with strong phase association to the LFP. To confirm that the signals recorded using the Gr MEA on the hippocampal surface reflected activity within the CA1 network, we examined data recorded with multishank probes targeted to dorsal CA1, which enabled layer-specific resolution of high γ and MUA (Fig. 3B; Extended Data Fig. 3-1). We found that high γ and MUA displayed phase-association to the LFP in all layers of CA1 (Fig. 3C). To corroborate these observations, we found that the observed distributions of LFP phase values associated with detected high γ activity peak amplitudes were significantly different from randomly selected distributions of LFP phase values of equal size in both Gr MEA and multishank probe recordings (Fig. 3D). Similarly, we found that the observed distributions of LFP phase values associated with detected MUA were significantly different from randomly selected distributions of LFP phase values of equal size in both Gr MEA and multishank probe recordings (Fig. 3E). These observations were recapitulated in substantial fractions of Gr MEA and multishank probe channels over all seizures recorded (Extended Data Fig. 3-2).

Seizure discharges form traveling waves through the CA1 network

Beyond the scales of single and ensembles of cells, network dynamics are thought to be important drivers of seizure activity (Schevon et al., 2012; Martinet et al., 2017; Driscoll et al., 2021). In addition to enabling imaging of

local populations of CA1 PCs and recording at single sites on the surface of CA1, the Gr MEA configuration allowed us to resolve network activity during seizures. We examined the propagation of individual seizure discharges across the CA1 surface in the Gr MEA recordings. Analysis of individual seizure discharges in the LFP robustly revealed variable latencies across the Gr MEA (Fig. 4A). To quantify the speed and direction of the traveling wave, we modified an analysis originally developed to map traveling waves across Utah array recordings from human epilepsy patients. In this paradigm, each seizure discharge was treated as a 3D data point (x , y , t), where the x - and y -coordinates corresponded to the spatial location in the 2D Gr MEA plane and t corresponded to the time of the peak LFP amplitude during a seizure discharge. We grouped data points based on their temporal proximity to each other (see Materials and Methods) to capture the propagation of single discharges across the MEA. The traveling wave direction was determined by the gradient direction of the plane, and the traveling wave speed was determined by the inverse of the gradient norm.

In the three animals with high quality Gr MEA recordings, we found that the direction of the seizure traveling wave was highly non-uniform ($p < 0.0001$ by the Omnibus test; Fig. 4B) and was distributed differently among animals ($p < 0.0001$ by pairwise Kolmogorov–Smirnov tests; Fig. 4B). While there was significant inter-animal variability, the traveling wave directions between seizures were highly consistent within individual animals (Extended Data Fig. 4-1). Moreover, we found that the directions of seizure onset captured via calcium were consistent with the distributions of seizure traveling wave direction (Extended Data Fig. 4-2). To examine the evolution of the traveling wave speed throughout the seizure, we compared the distributions of seizure discharge speeds from the first 25% of discharges versus the last 25% of discharges using a Mann–Whitney U test for each individual seizure (Fig. 4C). In the majority (9/12) of individual seizures, we found that the last 25% of discharges had a significantly lower median speed compared with the first 25% of discharges in a seizure. In the figure shown, the median speed in the first 25% of discharges was 0.4856 m/s, and the median speed in the last 25% of discharges was 0.4273 m/s. In the remaining 3/12 individual seizures, no difference was uncovered between the two distributions of speeds.

Relating single site, multimodal features to the traveling wave speed via bootstrap aggregated regression trees

Our technique allows us to observe hippocampal activity across two modalities (calcium imaging and electrophysiology) and multiple scales (single cells, cell ensembles, and network activity). To synthesize these data, we examined whether we could predict the traveling wave speed across individual seizures using features derived from single site electrophysiology and imaging of individual PCs under the putative site of recording. Towards this end, we extracted 10 time-varying features (five features per modality, 4-s duration sliding window with 1-s overlap)

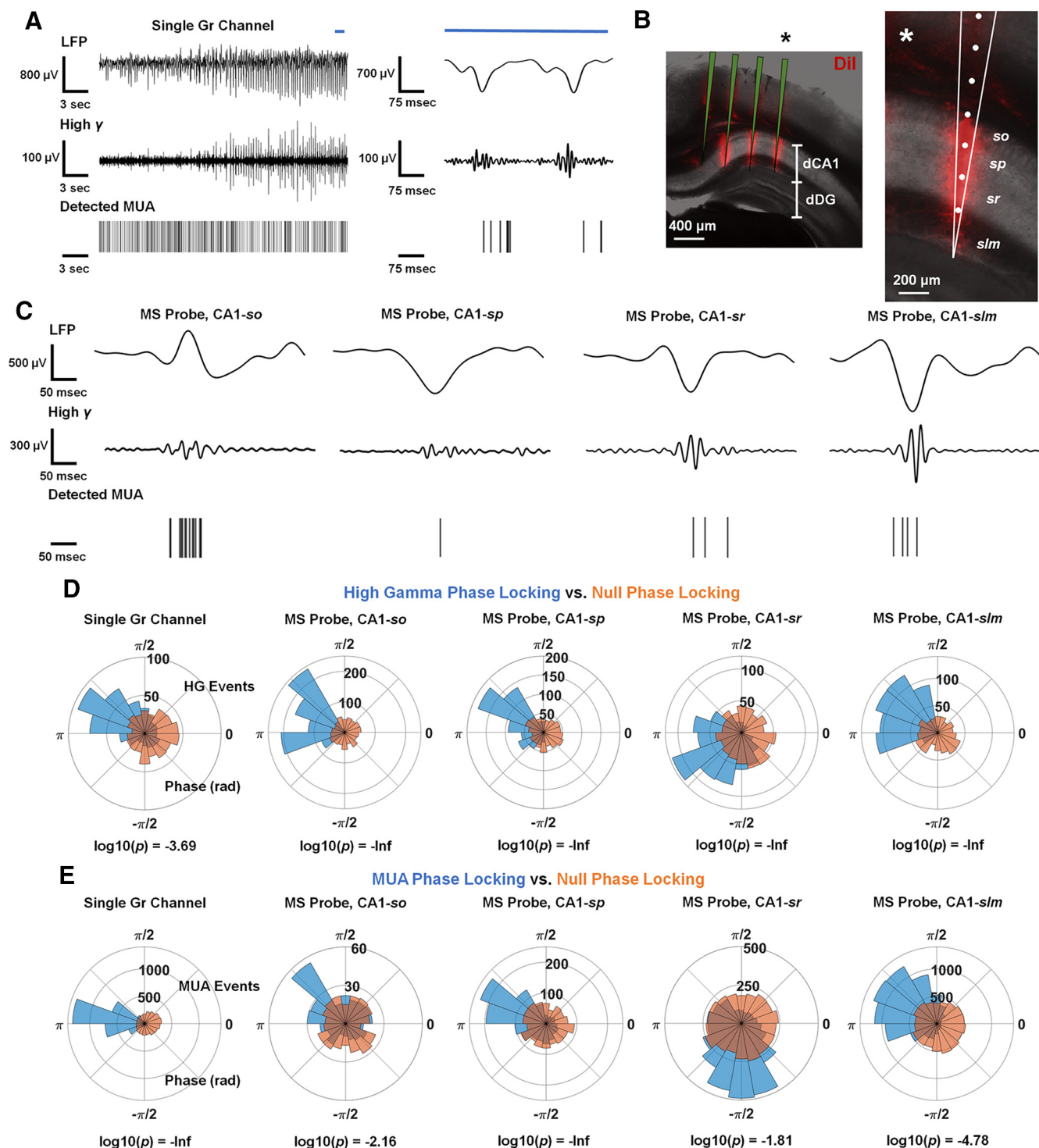


Figure 3. LFP-phase associated high γ and MUA emerge in CA1 during seizure. **A**, High γ and MUA with phase-association to the low-frequency component of the seizure appear in recordings made with the Gr MEA. Exemplar traces of seizure discharges (shown in the LFP), with concomitant high γ activity and detected MUA. A segment from the established seizure (blue line) is magnified on the right to show the phase-association behavior of γ and MUA (Extended Data Fig. 3-1). **B**, Location of a multishank probe implanted in dorsal CA1 (dCA1). The dorsal dentate gyrus is labeled as dDG. The placement of the rightmost shank, indicated with an asterisk, is magnified in the right panel. **C**, High γ and MUA with phase-association to the low-frequency component of the seizure appear in all layers of CA1. Exemplar traces of seizure discharges (shown in the LFP), with concomitant high γ activity and detected MUA. **D**, Polar histograms of exemplar phase distributions of detected peak high γ amplitudes from a single Gr microelectrode and microelectrodes located in the layers of CA1, shown in blue. Null distributions of randomly selected phase values are shown in orange. Log10-transformed p values shown are from the Watson-Williams test or the circular multisample test for equal

continued

median directions comparing the two displayed distributions (Extended Data Fig. 3-2). **E**, Polar histograms of exemplar phase distributions of detected MUA from a single Gr microelectrode and microelectrodes located in the layers of CA1, shown in blue. Null distributions of randomly selected phase values are shown in orange. Log10-transformed p values shown are from the Watson-Williams test or the circular multisample test for equal median directions comparing the two displayed distributions.

from four seizures with uninterrupted multimodal data (Materials and Methods). We trained 1000 bootstrap aggregated (bagged) regression tree ensembles on data from three of the four seizures to predict traveling wave speed from single site multimodal features (Fig. 5A). We found that the 1000 bagged regression trees could predict the traveling wave speed in the training datasets to a median Pearson's r of 0.7699 between experimental and

predicted median speed time series (Fig. 5B). The most important features in the 1000 bagged regression tree ensembles were mean fluorescence amplitude, mean calcium imaging line length (a measure of signal complexity), and mean high γ amplitude (Fig. 5C; Extended Data Fig. 5-1). When we made predictions on a fourth, withheld, seizure, we found that the top 10% of generalizable bagged regression trees predicted the traveling

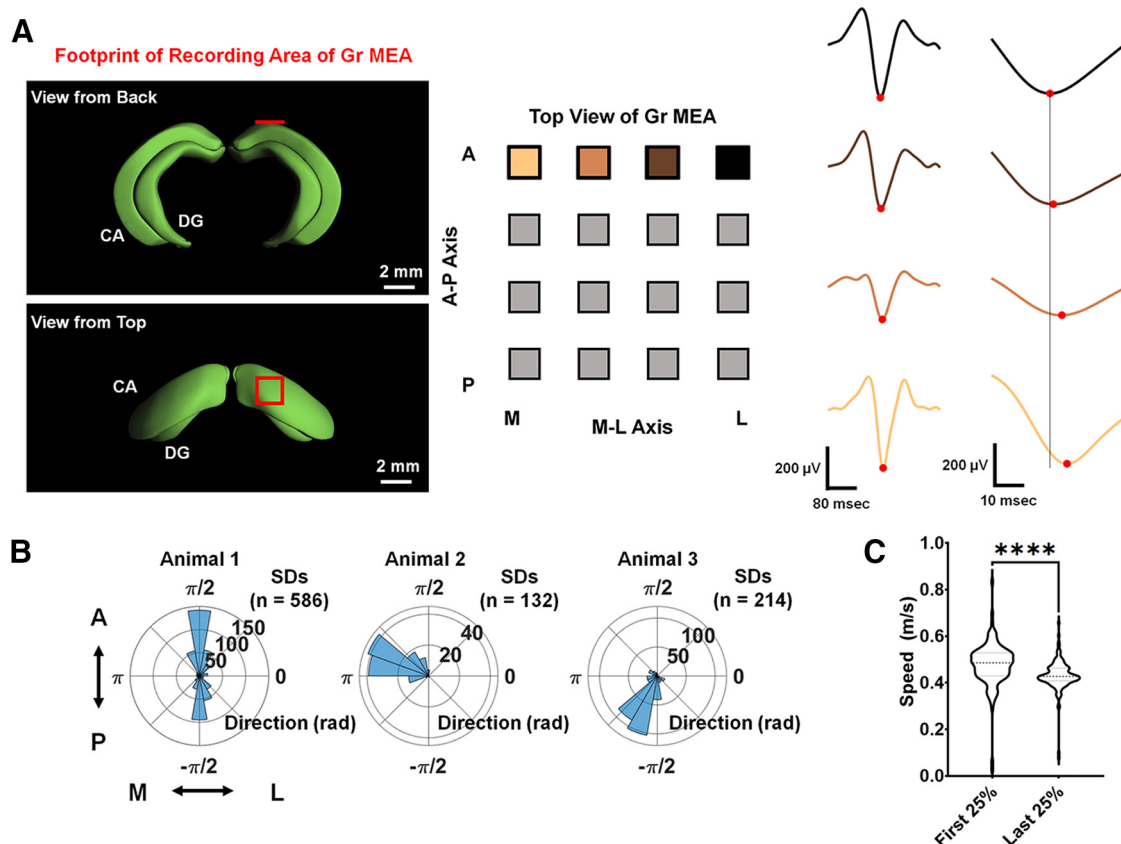


Figure 4. The low-frequency component of the seizure discharge is a traveling wave with variable direction and speed. **A**, The peak amplitude of the seizure discharge has variable latency across the Gr MEA. Left, Anatomical location of the recording area of the Gr MEA relative to the cornu ammonis (CA) and dentate gyrus (DG). Anatomical images courtesy of the Allen Brain Atlas 3D Viewer. Center, The footprint of the Gr MEA corresponding to the seizure discharge shown at right, with four electrode positions color coded as in the LFP trace. The horizontal axis corresponds to the medial-lateral (M-L) axis, with the most lateral channels located on the right of the panel, and the vertical axis corresponds to the anterior-posterior (A-P) axis, with the most anterior channels located on the top of the panel. Right, Recording of one representative discharge from four channels on a Gr MEA, with the peak amplitudes indicated with red dots. The earliest discharge is in black, and later discharges are in lighter colors. The rightmost portion of the panel displays a magnified view of the peak, with a vertical line to guide the eye and highlight the differences in peak latencies. **B**, Distributions of traveling wave directions in the three animals with high-quality Gr MEA recordings, displayed as polar histograms. In these plots, the angle corresponds to the direction of the gradient vector, and the radius corresponds to the number of seizure discharges (SDs) observed in the seizure. The arrow guide adjacent to the left most polar histogram provides an orientation of the plots along the A-P and M-L axes. (Extended Data Figs. 4-1, 4-2). **C**, Violin plots displaying the distributions of discharge speeds in the first 25% of a single seizure relative to the last 25% of a single seizure. The speed of the traveling wave decreases significantly in the last 25% of the seizure relative to the first 25% of the seizure (Mann-Whitney U test, $U = 4799$, **** $p < 0.0001$ for the comparison shown).

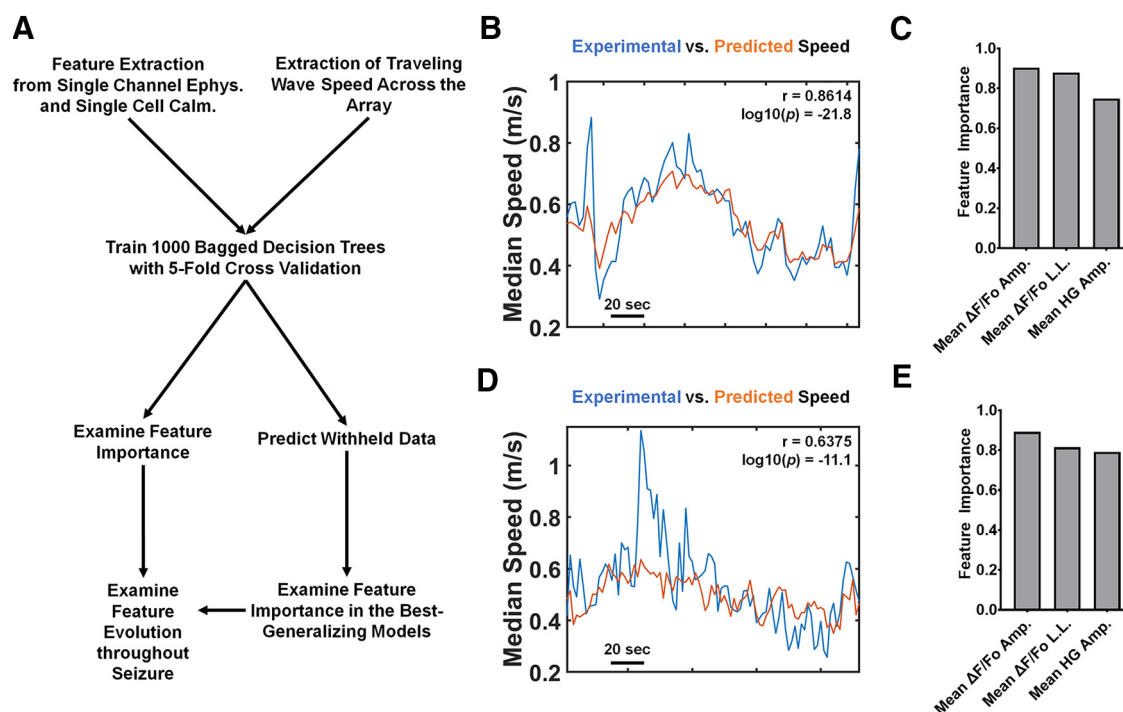


Figure 5. Prediction of seizure discharge traveling wave speed with single site, multimodal features using bootstrapped aggregated (bagged) regression trees. **A**, Simplified workflow detailing the machine learning experiment. Following the extraction of multimodal features from single channel electrophysiology and multicellular calcium imaging and the extraction of the traveling wave speed across the Gr MEA, we trained 1000 bagged regression trees with 5-fold cross validation. We examined feature importance across the 1000 models, and after predicting the traveling wave speed in a withheld dataset, examined feature importance in the best-generalizing models (Extended Data Fig. 5-1). Regression trees trained on multimodal features outperformed trees trained on single modality features (Extended Data Fig. 5-2). **B**, Prediction of traveling wave speed in a single seizure included in the training dataset. The experimentally observed traveling wave speed is displayed in blue, and the predicted traveling wave speed is displayed in orange. The Pearson's r value between the two series is 0.8614, with $\log_{10}(p) = -21.8$. **C**, Bar plot displaying the three most important features in the population of 1000 bagged regression trees. A representative image of the time evolution of the three most important features throughout a seizure is displayed in Extended Data Figure 5-3. In descending order of importance, they are the mean cellular $\Delta F/Fo$ amplitude (mean $\Delta F/Fo$ amp.), mean cellular $\Delta F/Fo$ line length (mean $\Delta F/Fo$ L.L.), and the mean high γ amplitude (mean HG amp.; Extended Data Fig. 5-1). **D**, Prediction of traveling wave speed in a seizure withheld from the training dataset. The experimentally observed traveling wave speed is displayed in blue, and the predicted traveling wave speed is displayed in orange. The Pearson's r value between the two series is 0.6375, with $\log_{10}(p) = -11.1$. **E**, Bar plot displaying the three most important features in the 100 best (top 10%) generalizing bagged regression trees. In descending order of importance, they are the mean cellular $\Delta F/Fo$ amplitude (mean $\Delta F/Fo$ amp.), mean cellular $\Delta F/Fo$ line length (mean $\Delta F/Fo$ L.L.), and the mean high γ amplitude (mean HG amp.; Extended Data Fig. 5-1).

wave to a median Pearson's r of 0.6208 between experimental and predicted median speed time series (Fig. 5D). The most important features in the best-generalizing models were mean fluorescence amplitude, mean calcium imaging line length, and mean high γ amplitude (Fig. 5E; Extended Data Fig. 5-1). Furthermore, we found that the trees trained on multimodal features outperformed trees trained on features derived from only one modality in predicting training and withheld data (Extended Data Fig. 5-2). The median Pearson's r values between predicted and true training traveling wave data were 0.7322 and 0.7127 for trees trained on calcium imaging and electrophysiology only features, respectively. These values differed significantly compared with the median Pearson's r of 0.7699 for predicting training and withheld data in multimodal regression trees (Extended Data Fig. 5-2A). For the top 100 generalizing models, the median Pearson's r values between true and predicted withheld traveling wave data were

0.4824, 0.5880, and 0.6208 for calcium imaging only, electrophysiology only, and multimodal regression trees (Extended Data Fig. 5-2B). The performance of the different models in predicting withheld data all differed significantly to $p < 0.01$.

Recalling that the speed of the traveling wave tends to be slower in the last 25% of discharges relative to the first 25% (Fig. 4C), we hypothesized that the three most important features would differ in the first 25% versus the last 25% of speed bins. We rescaled the mean fluorescence amplitude, mean calcium imaging line length, and mean high γ amplitude in these three seizures (Extended Data Fig. 5-3) and pooled the features from the first 25% versus the last 25% of each seizure. We found that the mean fluorescence amplitude was substantially lower in the last 25% of the seizure relative to the first 25% ($p < 0.0001$ by the Mann-Whitney U test; Fig. 6A). Similarly, we found that the mean calcium imaging line length was substantially lower in the last 25% of the seizure relative to the first 25%

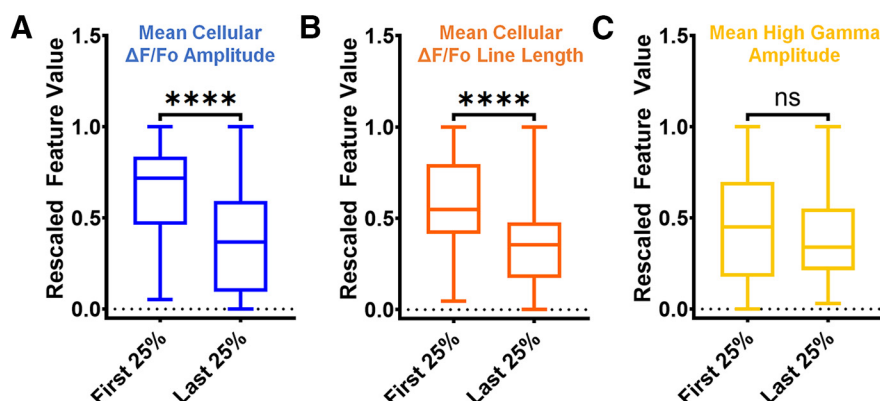


Figure 6. Comparison of pooled ($n=3$ seizures), rescaled values of the three most important features in the first 25% of seizure duration versus the last 25% of seizure duration. **A**, Mean cellular $\Delta F/Fo$ amplitude significantly decreases in the last 25% of seizure duration relative to the first 25% (Mann–Whitney U test, $U=1886$, **** $p < 0.0001$). **B**, Mean cellular $\Delta F/Fo$ line length significantly decreases in the last 25% of seizure duration relative to the first 25% (Mann–Whitney U test, $U=2159$, **** $p < 0.0001$). **C**, Mean high γ amplitude does not differ in the last 25% of seizure duration relative to the first 25% (Mann–Whitney U test, $U=3545$, $nsp > 0.05$). A summary of all analyses can be found in Extended Data Figure 6-1.

($p < 0.0001$ by the Mann–Whitney U test; Fig. 6B). Finally, we uncovered no difference between the mean high γ amplitude in the two epochs (Fig. 6C).

Discussion

Experimental considerations

Performing simultaneous, multimodal measurements of neural activity remains a substantial challenge in neuroscience. Combining modalities can provide different perspectives on, and thus a more comprehensive view of, neural activity (Lu et al., 2021). Moreover, multimodal measurements can overcome the drawbacks of single modalities and enable observations across scales, from single cells to networks. A summary of the analyses of our study can be found in Extended Data Figure 6-1. Our study was made possible by optically transparent MEAs based on graphene. First developed in 2014, multimodal measurements with Gr MEAs have been demonstrated in hippocampal slices *in vitro* (Kuzum et al., 2014) and *in vivo* in mouse cortex with low-magnification calcium imaging (Driscoll et al., 2021). We adapt the same MEA technology used in Driscoll's study by incorporating it into a cannula/imaging window assembly, and we implant it in the hippocampus, rather than cortex. Our study represents an advance relative to this previous work as we performed two-photon multicellular calcium imaging of defined neuronal populations in CA1 and extracellular electrophysiology of neural ensembles and the CA1 network. Critically, this multimodal paradigm enables us to monitor seizure activity across these scales.

Consistent with previous *in vivo* seizure imaging studies in cortex, we induced seizures in anesthetized animals during our experiments (Wenzel et al., 2017, 2019; Liou et al., 2018). Performing experiments under anesthesia reduced the animal burden of an hours-long evolution of epileptic activity. Indeed, anesthesia may change an animal's seizure threshold or seizure propagation speed relative to wakefulness, but importantly, seizures in humans also may occur under deep

anesthesia in the operating room or the medical intensive care unit (Wenzel et al., 2017, 2019). To induce seizures in our experiments, we bath applied 4-AP to the cortical surface contralateral to the site of hippocampal recording and imaging. Inducing seizures in this manner minimized disturbances to the objective lens of the two-photon microscope. After applying 4-AP contralateral to the site of imaging and recording, we observed epileptiform activity including spikes and extended epileptiform patterns in half of our experiments, consistent with clinical observations that epileptiform activity in patients with MTLE may occur hours before the clinical onset of seizures (Litt et al., 2001). Furthermore, when the hippocampus seized, we observed seizures of hypersynchronous onset, a typical pattern of seizure onset in MTLE patients (Weiss et al., 2016). One important caveat of our model is that while CA1 may receive seizure-promoting input from the entorhinal cortex or CA3, the global site of seizure induction is not in the hippocampal formation or the extended limbic system. The global site of seizure induction is the cortex contralateral to the hippocampus under recording and imaging. Models exploiting focal uncaging/application of convulsants (Miri et al., 2018) or stereotactically targeted electrical kindling (Takeuchi et al., 2021) may better recapitulate this feature of MTLE, although seizure initiation sites within single animals are highly variable in naturalistic models of MTLE (Toyoda et al., 2013).

Hippocampal versus cortical seizures

While hippocampal seizures *in vivo* have been understudied, our understanding of focal cortical seizures has advanced rapidly in the last 15 years (Schevon et al., 2019). Our study reports multiple observations convergent with observations made in animal models and human recordings of focal cortical seizures. As has been observed in PCs of the cortex, we report that PCs in CA1 exhibit variable, or elastic, absolute recruitment durations and reliable patterns of recruitment between seizures in individual animals (Wenzel et al., 2017, 2019). The

relatively slow recruitment (1.2 s on average to traverse a $\sim 300\text{-}\mu\text{m}$ field, with speeds on the order of hundreds of $\mu\text{m/s}$) observed at seizure onset in multicellular imaging resembled the evolution of a putative ictal core territory previously shown in low-magnification calcium imaging experiments (Schevon et al., 2012, 2019; Liou et al., 2020; Driscoll et al., 2021). In addition, we find that high γ and MUA organizes around the phase of the low-frequency seizure discharge in all layers of CA1 (Schevon et al., 2012; Weiss et al., 2013, 2015). Measures derived from these band-specific activities, such as the “phase-locked high γ ” measure, have been proposed as biomarkers to determine cortical regions for resection during epilepsy surgery (Weiss et al., 2015).

At the network level, we observe highly non-uniform distributions of seizure discharge traveling wave directions, as has been reported in human cortical epilepsy recordings (Smith et al., 2016; Martinet et al., 2017). The speed of the seizure discharge traveling wave (on the order of tens of cm/s) was orders of magnitude faster than the speed of seizure onset propagation observed in calcium imaging, which is consistent with experimental data from human epilepsy recordings by Schevon et al. (2012) and the computational model of seizure propagation proposed by Liou et al. (2020). In our experiments, the distributions of the traveling wave direction differed between animals. This observation may reflect animal-specific differences in network connectivity. Indeed, previous work has suggested that neurons in the epileptic hippocampus that are highly correlated during non-seizure periods may form a strongly connected network that facilitates the propagation of epileptic activity (Neumann et al., 2017). One important divergent observation between our study and the cortical seizure literature is that the traveling wave tends to decrease in speed in the final 25% of the seizure duration relative to the first 25% of the seizure duration. At least two studies analyzing electrophysiological data from human cortical epilepsy patients reported an increase in the speed of the traveling wave as the seizure approaches termination (Smith et al., 2016; Liou et al., 2017). In cortical seizures, the increase in the traveling wave speed late in seizure is thought to reflect the instability of an “ictal wavefront.” This wavefront is a sharply demarcated ($<2\text{ mm}$ wide) region of the cortex with continuous multiunit firing that gives rise to rhythmic discharges across broad areas of the cortex and whose input sharply dissipates at seizure termination (Schevon et al., 2019). This difference between observed cortical and hippocampal traveling wave speeds might be because of regional differences in cellular and network architecture, species differences between rodent and human brains, or our pharmacological model of epilepsy. Nonetheless, our observation may be the result of a distinct network process that occurs at seizure termination in CA1 of the hippocampus.

Relating single-site multimodal features and array-wide traveling wave speed

While our implant strategy enabled observations of seizures at the levels of single PCs, ensembles of cells, and the CA1 network, relating observations of neural

activity across scales remains a substantial conceptual problem (Lu et al., 2021). Observing neural activity across scales allows for a more complete picture of the neural processes behind phenomena like seizures. Indeed, the advance of multimodal recording technologies requires a concomitant advance in the analytical techniques used to understand multimodal, multiscale data (Driscoll et al., 2021). We used a machine learning-based approach to synthesize our analyses of the multimodal data across multiple scales of neural activity. We used bagged regression trees to predict the speed of the seizure traveling wave from features derived from single channel electrophysiology and multicellular calcium imaging. We chose regression trees as our model paradigm because of the well-established nonlinear nature of multiscale phenomena in the brain (Eissa et al., 2017). Using bagged regression trees improved the likelihood of the models generalizing to data from a fourth seizure withheld from the training dataset. Yet, bagged regression trees remained interpretable by way of examining the feature importance across all models trained (Fig. 5C) and the best generalizing models (Fig. 5E). Importantly, bagged regression trees trained on multimodal features outperformed trees trained on features from only one modality (either calcium imaging or electrophysiology) in the prediction of both training and withheld data (Extended Data Fig. 5–2). This result provides direct evidence for the importance of combining features from multimodal modalities to construct interpretable models.

We hypothesized that examining the values of the most important features in the first 25% versus last 25% of time bins might reveal differences reflective of physiological changes related to the slowing of the traveling wave speed. Importantly, this hypothesis does not imply that a change in feature values has a direct causal relationship with the slowing of the seizure discharge traveling wave speed *in vivo*. The most important features were mean cellular $\Delta F/F_0$ amplitude, mean cellular $\Delta F/F_0$ line length, and mean high γ amplitude. Mean cellular $\Delta F/F_0$ amplitude reflects how much the cells fluoresce in a given window. Although the intracellular calcium levels during a seizure likely exceed the linear regime relating action potentials and calcium transients, changes in $\Delta F/F_0$ amplitude are likely reflective of changes in somatic calcium levels in PCs. Cellular $\Delta F/F_0$ line length is a feature calculated as the sum of the absolute value of the first derivative of the $\Delta F/F_0$ time series. The first derivative of the $\Delta F/F_0$ time series is sensitive to changes in the $\Delta F/F_0$ time series and is commonly used to detect calcium transient events (Trevelyan et al., 2006). This feature is sensitive to fluctuations in signal amplitude and signal frequency (Esteller et al., 2001). Finally, mean high γ amplitude is directly reflective of the amplitude of the 80- to 150-Hz filtered electrophysiological signal at a given time point.

Between the traveling wave speed analysis (Fig. 4D) and the feature analyses (Fig. 6), we noted four co-incident observations between the first 25% and last 25% of the seizure duration: the traveling wave speed tends to decrease, the mean cellular $\Delta F/F_0$ amplitude feature

values decrease, the mean cellular $\Delta F/F_0$ line length feature values decrease, and the high γ amplitude values remain the same. To interpret this result, we noted multiple convergent threads of evidence from the seizure literature and our experiments. (1) Discharge traveling wave speed in models of cortical seizures is controlled by feedforward inhibition: epileptiform activity propagates slowly when inhibition is intact and quickly when inhibition is compromised (Trevelyan et al., 2006, 2007). (2) Synaptic inhibition from parvalbumin (PV-) and somatostatin-expressing (SST-) interneurons remains intact through the pre-seizure and early seizure phases (Miri et al., 2018). (3) Fast-spiking interneurons are thought to fire in structured temporal sequences during individual seizure discharges in the epileptic hippocampus (Neumann et al., 2017). (4) In our multishank probe experiments, we noted the presence of phase-associated multiunit firing and high γ activity in the interneuron-dominant strata oriens, radiatum, and lacunosum moleculare of CA1 (Fig. 2C). Taken together, the co-incidence of the reduction of traveling wave speed, reduction in calcium imaging feature values, and maintenance of the high γ amplitude may represent a late-seizure, local inhibition-dominant network state that restrains the seizure and facilitates to the transition to the postseizure state.

Limitations and outlook

Our results suggest a dynamic interplay between PC activity and the inhibitory network of CA1 in the transition from seizure to a postseizure state. A natural extension of this work is thus to induce seizures and perform simultaneous electrophysiological recordings and multicellular calcium imaging experiments in mice with calcium indicators targeted to genetically defined populations of hippocampal interneurons. Furthermore, using chronic seizure models that recapitulate the underlying pathophysiology and state dependence of seizure occurrence in MTLE may offer more naturalistic views of seizure dynamics (Ewell et al., 2015; Kahn et al., 2019).

Ultimately, three important themes emerge from the analyses of our study. First, our Gr MEA/imaging window/cannula assembly enables otherwise intractable cross-modal, cross-scale measurements in CA1 of the hippocampus. Next, hippocampal and cortical seizures may exhibit similar phenomena at the scales of individual cells and neural ensembles but different phenomena at the network scale. Finally, drawing on the results of our data reduction and machine learning experiments, CA1 may transition among states as seizures evolve toward termination.

References

- Ang CW, Carlson GC, Coulter DA (2006) Massive and specific dysregulation of direct cortical input to the hippocampus in temporal lobe epilepsy. *J Neurosci* 26:11850–11856.
- Berens P (2009) CircStat: a MATLAB Toolbox for circular statistics. *J Stat Softw* 31.
- Chen S, Su H, Yue C, Remy S, Royeck M, Sochivko D, Opitz T, Beck H, Yaari Y (2011) An increase in persistent sodium current contributes to intrinsic neuronal bursting after status epilepticus. *J Neurophysiol* 105:117–129.
- Driscoll N, Rosch RE, Murphy BB, Ashourvan A, Vishnubhotla R, Dickens OO, Johnson ATC, Davis KA, Litt B, Bassett DS, Takano H, Vitale F (2021) Multimodal in vivo recording using transparent graphene microelectrodes illuminates spatiotemporal seizure dynamics at the microscale. *Commun Biol* 4:136.
- Dulla CG, Janigro D, Jiruska P, Raimondo JV, Ikeda A, Lin CK, Goodkin HP, Galanopoulou AS, Bernard C, de Curtis M (2018) How do we use in vitro models to understand epileptiform and ictal activity? A report of the TASK1-WG4 group of the ILAE/AES Joint Translational Task Force. *Epilepsia Open* 3:460–473.
- Eissa TL, Dijkstra K, Brune C, Emerson RG, van Putten MJAM, Goodman RR, McKhann GM, Schevon CA, van Drongelen W, van Gils SA (2017) Cross-scale effects of neural interactions during human neocortical seizure activity. *Proc Natl Acad Sci USA* 114:10761–10766.
- England MJ, Liverman CT, Schultz AM, Strawbridge LM (2012) Epilepsy across the spectrum: promoting health and understanding. A summary of the Institute of Medicine report. *Epilepsy Behav* 25:266–276.
- Esteller R, Echaz J, Tchong T, Litt B, Pless B (2001) Line length: an efficient feature for seizure onset detection. *Annu Int Conf IEEE Eng Med Biol* 2:1707–1710.
- Ewell LA, Liang L, Armstrong C, Soltész I, Leutgeb S, Leutgeb JK (2015) Brain state is a major factor in pre-seizure hippocampal network activity and influences success of seizure intervention. *J Neurosci* 35:15635–15648.
- Farrell JS, Nguyen QA, Soltész I (2019) Resolving the micro-macro disconnect to address core features of seizure networks. *Neuron* 101:1016–1028.
- Jensen MS, Yaari Y (1997) Role of intrinsic burst firing, potassium accumulation, and electrical coupling in the elevated potassium model of hippocampal epilepsy. *J Neurophysiol* 77:1224–1233.
- Kahn JB, Port RG, Yue C, Takano H, Coulter DA (2019) Circuit-based interventions in the dentate gyrus rescue epilepsy-associated cognitive dysfunction. *Brain* 142:2705–2721.
- Kuzum D, Takano H, Shim E, Reed JC, Juul H, Richardson AG, de Vries J, Bink H, Dichter MA, Lucas TH, Coulter DA, Cubukcu E, Litt B (2014) Transparent and flexible low noise graphene electrodes for simultaneous electrophysiology and neuroimaging. *Nat Commun* 5:5259.
- Lévesque M, Shiri Z, Chen LY, Avoli M (2018) High-frequency oscillations and mesial temporal lobe epilepsy. *Neurosci Lett* 667:66–74.
- Liou JY, Smith EH, Bateman LM, McKhann GM, Goodman RR, Greger B, Davis TS, Kellis SS, House PA, Schevon CA (2017) Multivariate regression methods for estimating velocity of ictal discharges from human microelectrode recordings. *J Neural Eng* 14:e044001.
- Liou JY, Ma H, Wenzel M, Zhao M, Baird-Daniel E, Smith EH, Daniel A, Emerson R, Yuste R, Schwartz TH, Schevon CA (2018) Role of inhibitory control in modulating focal seizure spread. *Brain* 141:2083–2097.
- Liou JY, Smith EH, Bateman LM, Bruce SL, McKhann GM, Goodman RR, Emerson RG, Schevon CA, Abbott LF (2020) A model for focal seizure onset, propagation, evolution, and progression. *Elife* 9:e50927.
- Litt B, Esteller R, Echaz J, D'Alessandro M, Shor R, Henry T, Pennell P, Epstein C, Bakay R, Dichter M, Vachtsevanos G (2001) Epileptic seizures may begin hours in advance of clinical onset: a report of five patients. *Neuron* 30:51–64.
- Liu X, Ren C, Lu Y, Liu Y, Kim JH, Leutgeb S, Komiyama T, Kuzum D (2021) Multimodal neural recordings with Neuro-FITM uncover diverse patterns of cortical-hippocampal interactions. *Nat Neurosci* 24:886–896.
- Lu HY, Lorenc ES, Zhu H, Kilmarx J, Sulzer J, Xie C, Tobler PN, Watrous AJ, Orsborn AL, Lewis-Peacock J, Santacruz SR (2021) Multi-scale neural decoding and analysis. *J Neural Eng* 18:045013.
- Martinet LE, Fiddymont G, Madsen JR, Eskandar EN, Truccolo W, Eden UT, Cash SS, Kramer MA (2017) Human seizures couple across spatial scales through travelling wave dynamics. *Nat Commun* 8:14896.

- Merricks EM, Smith EH, McKhann GM, Goodman RR, Bateman LM, Emerson RG, Schevon CA, Trevelyan AJ (2015) Single unit action potentials in humans and the effect of seizure activity. *Brain* 138:2891–2906.
- Miri ML, Vinck M, Pant R, Cardin JA (2018) Altered hippocampal interneuron activity precedes ictal onset. *Elife* 7:e40750.
- Neumann AR, Raedt R, Steenland HW, Sprengers M, Bzymek K, Navratilova Z, Mesina L, Xie J, Lapointe V, Kloosterman F, Vonck K, Boon P, Soltesz I, McNaughton BL, Luczak A (2017) Involvement of fast-spiking cells in ictal sequences during spontaneous seizures in rats with chronic temporal lobe epilepsy. *Brain* 140:2355–2369.
- Park DW, Schendel AA, Mikael S, Brodnick SK, Richner TJ, Ness JP, Hayat MR, Atry F, Frye ST, Pashaie R, Thongpang S, Ma Z, Williams JC (2014) Graphene-based carbon-layered electrode array technology for neural imaging and optogenetic applications. *Nat Commun* 5:5258.
- Quiroga RQ, Nadasdy Z, Ben-Shaul Y (2004) Unsupervised spike detection and sorting with wavelets and superparamagnetic clustering. *Neural Comput* 16:1661–1687.
- Schevon CA, Weiss SA, McKhann G Jr, Goodman RR, Yuste R, Emerson RG, Trevelyan AJ (2012) Evidence of an inhibitory restraint of seizure activity in humans. *Nat Commun* 3:1060.
- Schevon CA, Tobochnik S, Eissa T, Merricks E, Gill B, Parrish RR, Bateman LM, McKhann GM Jr, Emerson RG, Trevelyan AJ (2019) Multiscale recordings reveal the dynamic spatial structure of human seizures. *Neurobiol Dis* 127:303–311.
- Smith EH, Liou JY, Davis TS, Merricks EM, Kellis SS, Weiss SA, Greger B, House PA, McKhann GM 2nd, Goodman RR, Emerson RG, Bateman LM, Trevelyan AJ, Schevon CA (2016) The ictal wavefront is the spatiotemporal source of discharges during spontaneous human seizures. *Nat Commun* 7:11098.
- Takano H, Coulter DA (2012) Imaging of hippocampal circuits in epilepsy. In: Jasper's basic mechanisms of the epilepsies (Noebels JL, Avoli M, Rogawski MA, Olsen RW, Delgado-Escueta AV, eds). 4th Ed. Bethesda: National Center for Biotechnology Information.
- Takano H, McCartney M, Ortinski PI, Yue C, Putt ME, Coulter DA (2012) Deterministic and stochastic neuronal contributions to distinct synchronous CA3 network bursts. *J Neurosci* 32:4743–4754.
- Takeuchi Y, Harangozó M, Pedraza L, Földi T, Kozák G, Li Q, Berényi A (2021) Closed-loop stimulation of the medial septum terminates epileptic seizures. *Brain* 144:885–908.
- Toyoda I, Bower MR, Leyva F, Buckmaster PS (2013) Early activation of ventral hippocampus and subiculum during spontaneous seizures in a rat model of temporal lobe epilepsy. *J Neurosci* 33:11100–11115.
- Trevelyan AJ, Sussillo D, Watson BO, Yuste R (2006) Modular propagation of epileptiform activity: evidence for an inhibitory veto in neocortex. *J Neurosci* 26:12447–12455.
- Trevelyan AJ, Sussillo D, Yuste R (2007) Feedforward inhibition contributes to the control of epileptiform propagation speed. *J Neurosci* 27:3383–3387.
- Weiss SA, Banks GP, McKhann GM Jr, Goodman RR, Emerson RG, Trevelyan AJ, Schevon CA (2013) Ictal high frequency oscillations distinguish two types of seizure territories in humans. *Brain* 136:3796–3808.
- Weiss SA, Lemesiou A, Connors R, Banks GP, McKhann GM, Goodman RR, Zhao B, Filippi CG, Nowell M, Rodionov R, Diehl B, McEvoy AW, Walker MC, Trevelyan AJ, Bateman LM, Emerson RG, Schevon CA (2015) Seizure localization using ictal phase-locked high gamma: a retrospective surgical outcome study. *Neurology* 84:2320–2328.
- Weiss SA, Alvarado-Rojas C, Bragin A, Behnke E, Fields T, Fried I, Engel J, Staba R (2016) Ictal onset patterns of local field potentials, high frequency oscillations, and unit activity in human mesial temporal lobe epilepsy. *Epilepsia* 57:111–121.
- Wenzel M, Hamm JP, Peterka DS, Yuste R (2017) Reliable and elastic propagation of cortical seizures in vivo. *Cell Rep* 19:2681–2693.
- Wenzel M, Hamm JP, Peterka DS, Yuste R (2019) Acute focal seizures start as local synchronizations of neuronal ensembles. *J Neurosci* 39:8562–8575.
- Yaksi E, Friedrich RW (2006) Reconstruction of firing rate changes across neuronal populations by temporally deconvolved Ca²⁺ imaging. *Nat Methods* 3:377–383.